

Research Article

Water Transport in Unsaturated Cracked Concrete under Pressure

Yuanzhu Zhang¹, Siming Zhang¹, Gang Wei¹, Xinjiang Wei¹, Liqiao Jin², and Kuixin Xu³

¹School of Engineering, Zhejiang University City College, Hangzhou 310015, China

²College of Civil Engineering and Architecture, Zhejiang University, Hangzhou 310058, China

³School of Civil Engineering and Architecture, AnHui University of Science and Technology, Huainan 232001, China

Correspondence should be addressed to Yuanzhu Zhang; zhangyz@zucc.edu.cn

Received 12 February 2019; Revised 28 May 2019; Accepted 18 June 2019; Published 16 July 2019

Academic Editor: Robert Černý

Copyright © 2019 Yuanzhu Zhang et al. This is an open access article distributed under the Creative Commons Attribution License, which permits unrestricted use, distribution, and reproduction in any medium, provided the original work is properly cited.

In order to analyze the process of hydraulic water infiltrating cracked concrete of underwater tunnels, the equation of water transport in unsaturated cracked concrete under pressure was proposed according to the double-porosity medium model. Penetration tests on prefabricated cracked concrete blocks were conducted, and then the influence of hydraulic pressure, initial saturation, and crack width on water transport was studied. The results show that the larger the water pressure, the lower the initial saturation, and the wider the crack width, then the greater the penetration depth, which can be reasonably explained according to water motion theoretical models in this study. Moreover, the TOUGH2 software was used to simulate the change and distribution of saturation, driving potential, and water velocity of unsaturated cracked concrete, which further proved the experimental results and theoretical analysis. It reflects that both pressure potential and matric potential are the driving force of water transport in underwater cracked concrete, and the driving force will be converted with the change of concrete saturation. In addition, crack width is positively correlated with concrete permeability.

1. Introduction

For submerged constructions such as underwater tunnels which keep bearing high hydraulic pressure, it is a big challenge to prevent seepage in its service period. In fact, water seepage is a common risk for underwater tunnels. In China, the saying “nine out of ten tunnels will leak” reflects the severity of tunnel seepage. Long-term seepage of corrosive water not only threatens traffic safety but also results in a series of durability problems, such as concrete dissolution, concrete neutralization, reinforcement corrosion, and further expansion of cracks. For example, the rails in the Kanmon Tunnel in Japan are replaced every 5.8 years because of the corrosion by seepage salt water, which is much faster than the cycle of replacing (28 years) for mountain tunnels [1]. Thus, the owner has to spend huge amounts of money on maintenance to meet the requirement of service life [2]. It is reported that the annual cost of maintenance and the replacement cost for a tunnel could be as high as \$150 K/km and \$250 million/km in 1997 [3].

Thus, it is necessary to study the process of water transport in underwater concrete tunnels; moreover, two aspects should be taken into further considerations.

First, cracks are inevitable for underwater concrete tunnels due to temperature stress, shrinkage, load, uneven settlement, and so on. Because cracks provide fast pathways for water transport, since the 1990s, researchers began to carry out experiments to investigate the permeability of cracked concrete. Kermani [4] first pointed out that even microcracks can significantly affect the permeability of concrete in 1991. Subsequently, a large number of experiments found that crack opening (width) was a main factor on permeability of cracked concrete. For example, Gérard et al. [5] and Wang et al. [6] found that concrete permeability was basically the same as sound concrete when the crack opening is below $50\text{ }\mu\text{m} \sim 100\text{ }\mu\text{m}$; however, the permeability coefficient increased with the crack opening over than $100\text{ }\mu\text{m}$. Moreover, further experimental researches proved the permeability coefficient of cracked concrete is related to the square of crack

opening [7, 8], that is, the cubic law was applicable to cracked concrete.

On the other hand, permeability and capillary absorption are primary mechanisms for water transport in concrete. Permeability takes place in saturated pores filled with fluid whilst under external pressure, and driving force for permeability is the pressure gradient, which can be analyzed by Darcy's law. However, capillary absorption drives water transport in unsaturated concrete, which can be analyzed by Richards' equation. Some researchers also studied the effect of water pressure and capillary suction on water transport in cracked concrete. Yi proposed that the permeability of concrete increased dramatically with the crack width and hydraulic pressure when the water pressure is greater than 0.025 MPa [9]. Shin's experimental research suggests that the permeability coefficients are most influenced by water head and crack width [10]. Wang et al. [11] put forward a mesoscale model for cracked concrete based on the theory of unsaturated flow and cubic law, and then numerically analyzed the water content at the crack location. However, there are rare studies on combined transport of water in unsaturated cracked concrete under pressure and capillary suction up to now. In fact, water transport in concrete of the underwater tunnel is not only permeability but also capillary absorption. For the underwater concrete tunnel, the outer wall contacts with hydraulic water while the inner wall contacts with atmosphere. Hence, the pressure difference will drive the external water ingress into the tunnel from the outer wall to the inner wall. Meanwhile, cement-based materials are difficult to reach full saturation by analyzing the initial water content of concrete [12]. Recently, concrete coring tests of underwater constructions in Denmark showed that underwater concrete in service was still unsaturated except near-surface zone even for decades [13]. Hence, water transport in tunnel concrete should consider the unsaturated characters of concrete.

In this study, the equation of water transport in unsaturated cracked concrete under pressure was proposed based on the double-porosity medium model. Then, the influence of hydraulic pressure, initial saturation, and crack width on water transport was studied through permeability tests. The TOUGH2 software was used to simulate the saturation, driving potential, and water flow velocity of unsaturated cracked concrete. The research is helpful to improve the durability design of the underwater concrete tunnel.

2. Theoretical Basis

According to the double-porosity medium model [14], cracked concrete can be equivalent to two kinds of continuous porous media (concrete and fracture) with different hydraulic parameters; the porosity and permeability of fracture are much greater than those of concrete. Therefore, water transport in cracked concrete can be viewed as flow in sound concrete and flow through cracks.

Water movement in the unsaturated porous media could be described by Richards' equation as follows [15]:

$$u = -\frac{k_s k_r(\theta)}{\mu} \nabla \psi, \quad (1)$$

where u is the fluid velocity, m/s; k_s is the intrinsic permeability of porous media in saturated state, m^2 ; k_r is the relative hydraulic conductivity, and it ranges between 0 (dry state) and 1 (saturated state); θ is the water content; μ is the viscous dynamic coefficient of water, $\text{Pa}\cdot\text{s}$; ∇ is nabla operator; and ψ is the total driving potential of unit volume water, Pa.

k_r is a function of water content, which is commonly represented by the van Genuchten–Mualem model [16]:

$$k_r(s) = s^{0.5} \left[1 - \left(1 - s^{1/m} \right)^m \right]^2, \quad (2)$$

where s is the water saturation, $s = (\theta - \theta_r)/(\theta_s - \theta_r)$; θ_r is the residual water content; θ_s is the saturated water content; and m is an empirical parameter which can be fitted by experimental data.

The total driving potential ψ of water motion includes pressure potential ψ_p and matrix potential ψ_m . So here is

$$\psi = \psi_p + \psi_m. \quad (3)$$

Pressure potential ψ_p is caused by the difference of pressure in pressure field. Considering the connectivity of capillary pores, it is assumed that air in unsaturated pores directly connects with external atmosphere; thus, the pore solution in unsaturated zone is subjected to atmospheric pressure without additional hydrostatic pressure. However, the pore solution in the saturated zone directly connects with external hydraulic water, so it is subjected to the additional hydrostatic pressure which depends on surface pressure and location. Therefore, pressure potential can be calculated by the following equation [17]:

$$\begin{aligned} \psi_p &= 0, & 0 \leq s < 1, \\ \psi_p(x, t) &= P_0 \operatorname{erfc} \left(\frac{x}{2} \sqrt{\frac{\rho_w g}{K_s E t}} \right), & s = 1, \end{aligned} \quad (4)$$

where P_0 is the hydraulic pressure on tunnel outer surface, Pa; erfc is the complementary error function; x is the distance from the exposed surface, m; E is the bulk modulus, Pa; and t is the pressuring time, s.

Matrix potential ψ_m can be viewed as capillary suction of porous materials. It is negative and generally described by the van Genuchten–Mualem model as follows [16]:

$$\psi_m = -\alpha (s^{-1/m} - 1)^{1-m}, \quad (5)$$

where α is an empirical parameter fitted by experimental data.

For the underwater concrete tunnel, it is unsaturated in early service stage, and then with water transport, the saturation of concrete increases gradually to form saturated zone ($s=1$) and unsaturated zone ($s<1$). In the saturated zone, $\psi_m=0$ and $\psi_p>0$, while in unsaturated zone, $\psi_m<0$ and $\psi_p=0$. The main driving force for water transport is converted with the change of concrete saturation.

Hydraulic conductive of concrete with a parallel crack is usually determined according to the cubic law, which can lead to the following intrinsic coefficient [18]:

$$k_s^c = \frac{w^2}{12}, \quad (6)$$

where k_s^c is the intrinsic permeability coefficient of crack in saturated state, m^2 , and w is the crack width, m .

Combine formulas (1) and (6), so water motion equation of unsaturated crack can be described as

$$\dot{u}^c = -\frac{k_s^c k_r(\theta)}{\mu} \nabla \psi, \quad (7)$$

where u^c is the fluid velocity at crack, m/s .

At last, we combine motion equation of sound concrete (formula (1)) and crack (formula (7)) with mass conservation (equation (8)) to obtain governing equations of water transport in unsaturated cracked concrete under pressure, which can be solved by the finite difference method.

$$\frac{\partial(\phi s)}{\partial t} = -\operatorname{div}(u), \quad (8)$$

where ϕ is the porosity and div is the divergence.

3. Experimental Research

3.1. Test Block Preparation. Two kinds of test blocks were prepared according to the concrete mixture shown in Table 1, among which the concrete mixture of BI blocks was referred to that of Zhoushan Shenjiamen undersea tunnel in China. Ordinary Portland cement Grade 42.5 and fly ash Grade II were used as binder materials. Gravel with maximum particle size of 25 mm and river sand were used as coarse aggregate and fine aggregate, respectively. Polycarboxylic acid is used as the water-reducing agent.

The schematic diagram of the test block is shown in Figure 1. Considering the size limitations of the pressure chamber in our experiments, we set 150 mm height of the test block which can touch the cover plate tightly and a $\phi 6$ diameter hole at the bottom of the block to align with the water outlet of the pressure chamber. Meanwhile, the prefabricated crack is arranged along the block axis which is not connected up and down, so as to avoid water seepage directly from the top of the test block. In addition, in order to improve the production efficiency, the test block was made by a 150 mm cube mould; an 8 mm thick smooth slab was inserted on the axis of the mould, so as to make two blocks at the same time. When prefabricating the hole and cracks, we first located the hole and crack position and then inserted a $\phi 6$ steel bar and stainless steel sheets into the predetermined location (Figure 2). The width of the stainless steel sheet determines the crack length of prefabricated specimens ($l = 30 \text{ mm}$ for each side), and the thickness of the stainless steel sheet determines the crack width of the prefabricated specimens. After layered pouring of concrete into the mould, we pulled the stainless mould out smoothly before concrete

TABLE 1: Concrete mixture.

Number	w/b	Mix proportion ($\text{kg}\cdot\text{m}^{-3}$)				
		Cement	Fly ash	Sand	Gravel	Reducer
BI	0.33	456	44	640	1253	163
BII	0.43	349	39.8	548.8	1266.5	167.6
						4.6
						3.49

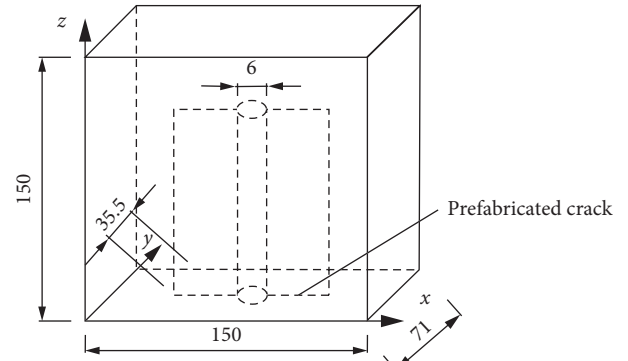


FIGURE 1: Concrete block schematic (unit: mm).

initial coagulation. Two days later, the mould was removed and the test blocks were sent to cure in a standard curing box (temperature $20^\circ\text{C} \pm 2^\circ\text{C}$ and relative humidity above 95%) for 28 d.

Before penetration tests, the fractures on the bottom surface were sealed with epoxy glue, in order to keep the prefabricated hole as the only inlet (Figure 3). Hence, the inner side of the block is equivalent to the outer wall of the underwater tunnel bearing hydraulic pressure. However, the outer side of the block directly contacts with atmosphere without seal, which is equivalent to the inner wall of the underwater tunnel bearing atmospheric pressure.

After the tests are completed, the test blocks were split on the universal testing machine (UTM) to measure the actual crack widths by FTLF-2 crack width measuring instrument (range: 8 mm; accuracy: 0.01 mm). It is found that the actual crack widths of all working conditions fluctuate near the prefabricated widths, and this is because the concrete is disturbed and then closed when the steel sheets are pulled out. Hence, we carefully chose the experimental results of well-made blocks to analyze, which means that the error values of prefabricated crack widths are not more than 0.1 mm. In general, the prefabrication error of crack width $w = 0.3 \text{ mm}$ is less than that of $w = 0.1 \text{ mm}$ and $w = 1 \text{ mm}$.

3.2. Laboratory Tests

3.2.1. Strength, Porosity, and Saturated Hydraulic Conductivity. The cube compressive strength ($f_{cu,k}$), porosity (ϕ), and saturated hydraulic conductivity (K_s) of the concrete blocks were determined according to *Standard for test method of mechanical properties on ordinary concrete* (GB/T 50081-2002) [19], *Standard test method for density, absorption, and voids in hardened concrete* (ASTM C642-13) [20], and *Test*

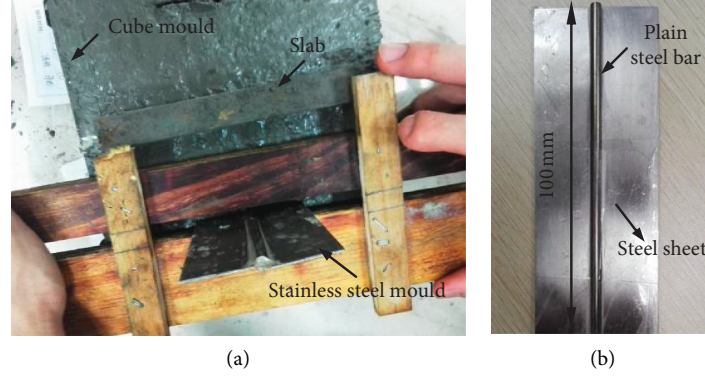


FIGURE 2: Cracked block preparation: (a) cube mould; (b) stainless steel mould.



FIGURE 3: Sealing of the cracks on the specimen bottom.

code for hydraulic concrete (SL352-2006) [21], respectively. The test results are shown in Table 2. In addition, the relationship between saturated hydraulic conductivity and intrinsic permeability coefficient in Section 2 satisfies the following formula:

$$k_s = \frac{K_s \mu}{\rho_w g}. \quad (9)$$

3.2.2. Initial Saturation of the Specimens. In order to analyze the effect of matric potential on water transport in unsaturated concrete, three initial states were designed: natural state and oven-dried at 105°C for 0.5 h and 8 h.

First, the mass of the concrete test block was measured by using an electronic balance as the initial mass m_0 in the natural state. Then, the test block was oven-dried at 105°C for 48 h to weigh the residual mass m_r . After that, the block was taken out from the oven and fully immersed into water. The mass of the block was measured daily until it became constant, and the constant mass was taken as fully saturated mass m_s . Then, the fully saturated blocks were, respectively, oven-dried for 0.5 h and 8 h, the mass of which were recorded as the initial mass m_0 in the other two states. Finally, initial saturation s_0 of the concrete blocks can be determined by formula (10), and the results are shown in Table 3. The initial saturation of both BI and BII test blocks in the natural state is about 0.7, which indicates that concrete blocks are unsaturated at the initial stage. Meanwhile, BI with lower w/b has a lower saturation than BII, because more water was consumed for hydration reaction with higher dosages of cement, correspondingly less water left in capillary pores after hydration.

TABLE 2: Strength, porosity, and saturated hydraulic conductivity of the blocks.

No.	$f_{cu,k}$ (MPa)	ϕ (%)	K_s ($m \cdot s^{-1}$)
BI	50.8	8.8	1.3×10^{-11}
BII	43.8	10.4	2.9×10^{-11}

TABLE 3: Initial saturation of the test blocks.

No.	Condition	s_0
BI-1	Natural state	0.70
BI-2	Oven-dried for 0.5 h	0.90
BI-3	Oven-dried for 8 h	0.30
BII-1	Natural state	0.72
BII-2	Oven-dried for 0.5 h	0.95
BII-3	Oven-dried for 8 h	0.32

$$s = \frac{m_0 - m_r}{m_s - m_r}. \quad (10)$$

3.3. Test Conditions and Test Procedure. The penetration tests were carried out by means of a pressure infiltration device shown in Figure 4, which is composed of a digital pressure control gauge, a pressure sensor, a booster pump, a stainless steel tank, pressure chambers, and pipelines. According to the survey of crack depths and the range of buried depth of underwater tunnels and service conditions of wetting and drying of concrete tunnels, the test conditions are set, as shown in Table 4.

Because the water content of concrete at each location is difficult to be directly detected by the current test instrument, only nuclear magnetic resonance (NMR) can determine the average water content of samples by measuring the content of H^+ in porous media at present [12]. Other experimental studies usually take water absorptions [22], neutron imaging [23, 24], and penetration depth [25] to deduce the infiltration process. Considering penetration depth is easy to observe and detect, we take it to analyze water transport in this paper.

When taking the penetration tests, the test procedure is as follows:

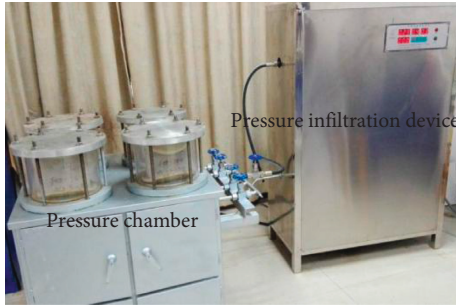


FIGURE 4: Experimental devices.

TABLE 4: Working conditions of the tests.

Conditions	w (mm)	P_0 (MPa)	s_0	Pressuring time (h)
1–4	0.5	0.1	0.70	12, 24, 48, 72
5–8	0.5	0.3	0.70	12, 24, 48, 72
9–12	0.5	0.4	0.70	12, 24, 48, 72
13–16	0.5	0.3	0.30	12, 24, 48, 72
17–20	0.5	0.3	0.90	12, 24, 48, 72
21–24	0.1	0.3	0.70	12, 24, 48, 72
25–28	0.3	0.3	0.70	12, 24, 48, 72
29–32	0.3	0.1	0.72	12, 24, 48, 72
33–36	0.3	0.3	0.72	12, 24, 48, 72
37–40	0.3	0.6	0.72	12, 24, 48, 72
41–44	0.3	0.3	0.32	12, 24, 48, 72
45–48	0.3	0.3	0.95	12, 24, 48, 72
49–52	0.5	0.3	0.72	12, 24, 48, 72
53–56	1.0	0.3	0.72	12, 24, 48, 72

- (1) First, align the prefabricated hole at the bottom of the test block with the outlet of the pressure chamber and then cover 2 cm thick stainless steel plate on the test block. Hereafter, press the cover plate with six steel rods to fix the specimen.
- (2) After that, set the pressure and pressuring time on the instrument control panel according to the working conditions and then open water valve and turn on the pressure infiltration device. The pressure pump will push the water in the tank into the concrete test block through the water outlet.
- (3) When the predetermined pressuring time is reached, turn off the valve of the tank and take out the test block from the pressure chamber. Then, use a universal testing machine to split the test block at $z = 50$ mm; finally, water penetration depth along and vertical to the crack was measured by a vernier caliper.

Since concrete itself is an inhomogeneous composite material, although we carefully make test blocks with a vibration table, the uniformity of coarse aggregate distribution and connected capillary pores distribution is hard to control. Because water transports only through connected capillary pores in concrete, the inhomogeneity of blocks will objectively affect the characteristics of water transport, but from the macroscale analysis, it is acceptable. This can be confirmed by the symmetrical distribution of our penetration depth maps.

In addition, when the cracks at the bottom of the test block are sealed, the sealing may be uneven due to the coating quality of epoxy glue. Therefore, we split the samples at $z = 50$ mm to avoid the adverse effects of uneven bottom sealing quality.

3.4. Results and Discussion

3.4.1. Penetration Depth of Cracked Concrete Specimens. From the penetration depth map of the split block in Figure 5, it can be seen that the seepage scope is spindle shaped around the cracks; meanwhile, the penetration depth along the crack direction is much larger than that in the vertical to crack direction, which reflects the permeability of cracked concrete is greater than that of sound concrete.

Taking the working conditions 1–4 as an example, we line water penetration depth along and vertical to crack directions in half of the test block at 12 h, 24 h, 48 h, and 72 h (Figure 6). It is found that the penetration depth increases with time in both directions and the penetration depth along the crack is essentially equal to the sum of crack length (30 mm) and the penetration depth in the vertical direction. It reflects that water rapidly reaches the end of the crack, which maybe because the crack length is small and the flow velocity is fast. In the subsequent analysis, the penetration depth along the crack direction is taken as the water penetration depth.

3.4.2. Influence of Water Pressure. From Figure 7 (1–12 conditions and 29–40 conditions), it is noted that penetration depth increases with external water pressure, while the increase of penetration depth under different water pressures is nonlinear, which reflects that external water pressure is not the only factor to drive water transport in cracked concrete. We take the experimental results of 1–12 conditions of BI blocks, for example, to explain the water infiltration process in cracked concrete based on our theoretical models:

- (1) When pressuring water infiltrates concrete through the hole and cracks, it is considered that there is a very thin fully saturated layer on the surface of the hole and cracks, so that the driving potential of this saturated surface layer is $\psi(x = 72 \text{ mm}, x = 78 \text{ mm}) = \psi_p = P_0$, while in the interior unsaturated concrete, it is $\psi(x < 72 \text{ mm} \text{ or } x > 78 \text{ mm}) = \psi_m = -12.9 \text{ MPa}$. As a consequence, the greater the P_0 is, the greater the $\nabla\psi$ will be (formula (3)). Hence, greater P_0 causes faster initial velocity u_0 on the saturated surface (formula (1)).
- (2) The faster the initial velocity u_0 , the faster the increase in saturation near the fully saturated surface and then the faster the change in the matric potential (formula (5)). Therefore, in the unsaturated zone, the greater the P_0 is, the greater the $\nabla\psi$ is. At the same time, the relative permeability coefficient k_r (formula (2)) increases with the saturation s . As a result, still in this stage, the greater the P_0 , the faster the flow velocity u and

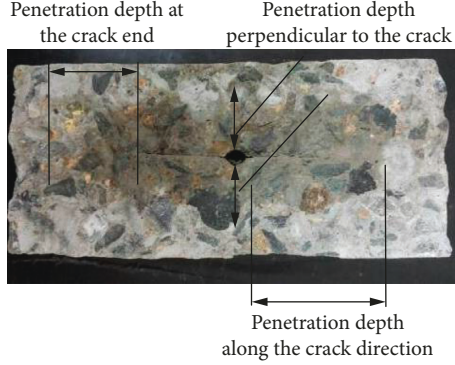


FIGURE 5: Penetration figure after concrete block splitting.

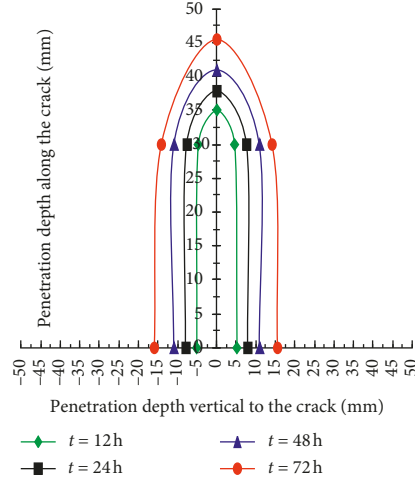


FIGURE 6: Penetration depth map of working conditions 1–4.

then the faster the increase in corresponding saturation s according to formula (1).

- (3) With increase in time, the specimen with greater P_0 gradually formed the fully saturated region ($s = 1$). At this time, the matric potential ψ_m increases to zero and driving potential of water motion is converted to pressure potential ψ_p . By applying formula (4), we can see that the greater the P_0 and t are, the greater the ψ_p is, so the velocity u in the saturated zone is also greater (Darcy's law), which results in faster saturation growth and more obvious difference with the initial saturation of the test block; hence, greater water penetration depth was shown on the test block.

Meanwhile, it is easy to notice that the penetration depths of B1 blocks are greater than those of BII blocks under the same pressure due to the wider cracks.

3.4.3. Influence of Initial Saturation. Figure 8 shows the penetration depth of cracked concrete blocks under different initial saturation conditions (conditions 5–8, 13–20, 33–36, and 41–48). It is noted that the lower initial saturation of concrete is, the greater penetration depth is, which reflects

that the matric potential (relative to initial saturation) is a driving force of water movement. Similarly, the penetration depth of the BI test block is larger than that of the BII test block because of wider crack width.

Taking an example of the BI blocks (Figure 8(a)), the experimental results are because that on the saturated layer of inlet ($x = 72\text{ mm}$, $x = 78\text{ mm}$), the total driving potential $\psi = \psi_p = 0.3\text{ MPa}$, while the total driving force of interior unsaturated is $\psi(x < 72\text{ mm} \text{ or } x > 78\text{ mm}) = \psi_m$. According to formula (5), the lower the initial saturation s_0 is, the lower the matric potential ψ_m will be (the absolute value is greater). Thus, $\nabla\psi = \psi(x = 72\text{ mm}) - \psi(x < 72\text{ mm})$ or $\nabla\psi = \psi(x = 78\text{ mm}) - \psi(x > 78\text{ mm})$ is greater. Therefore, the lower the initial saturation, the faster the water velocity according to formula (1), which then causes faster saturation growth and more obvious difference from the initial saturation of the test block; hence, water penetration depth is greater on the test block.

3.4.4. Influence of Crack Width. Figure 9 shows the penetration depth of cracked concrete blocks under different crack widths (conditions 5–8, 21–28, 33–36, and 49–56). It can be seen that the greater the crack width, the greater

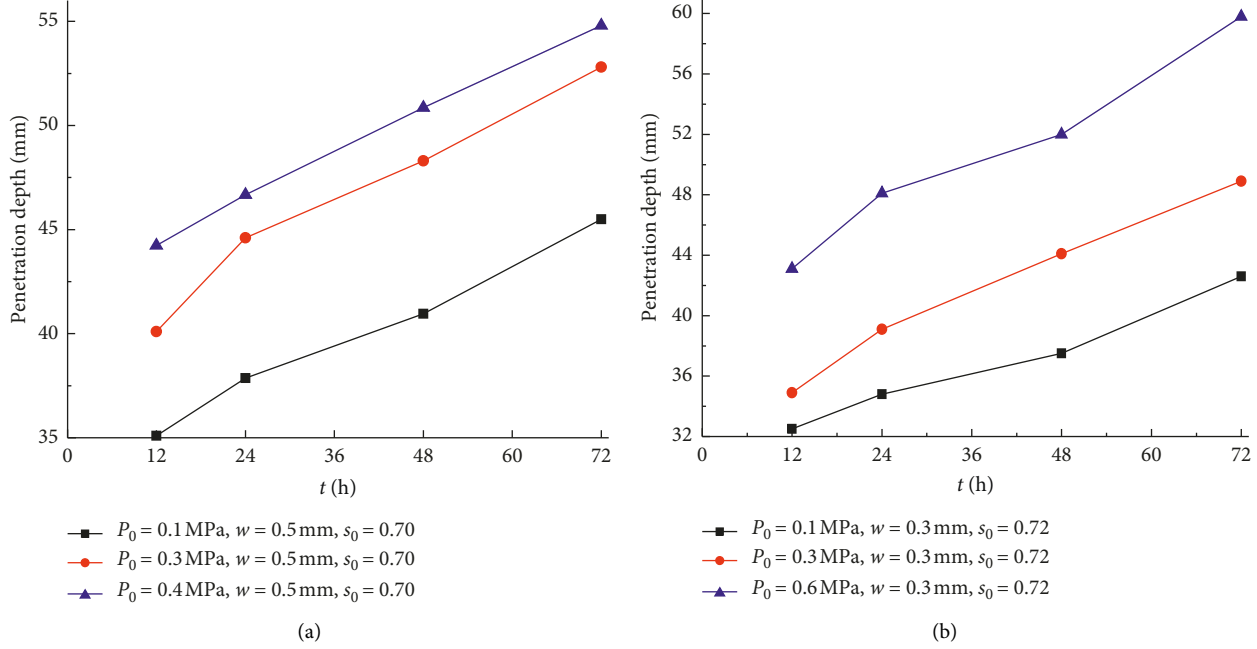


FIGURE 7: Penetration depth under different hydraulic pressures. (a) BI test blocks. (b) BII test blocks.

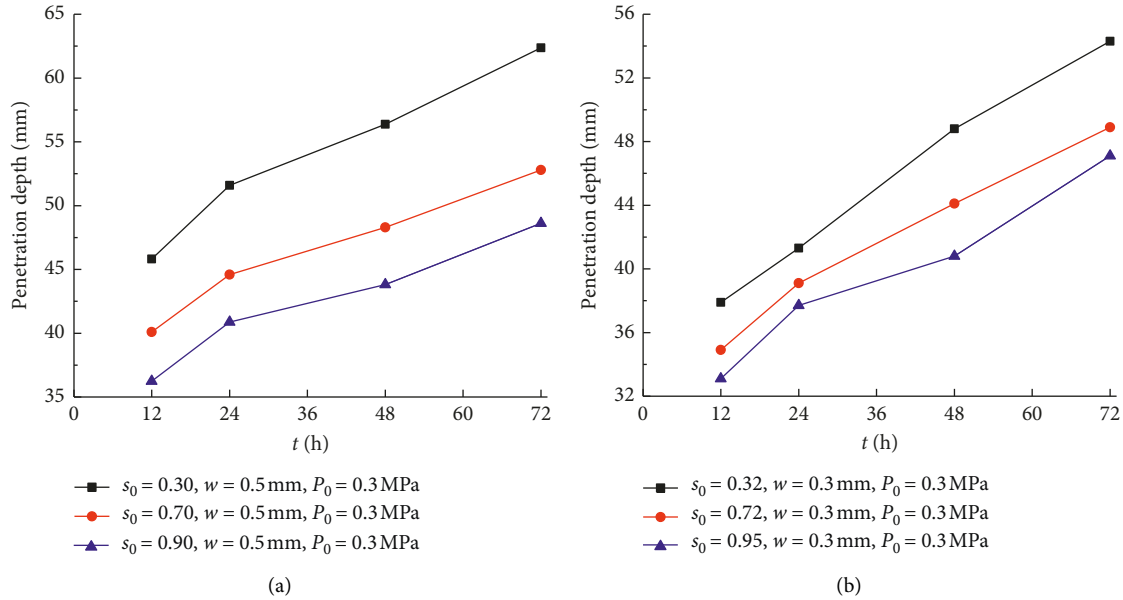


FIGURE 8: Penetration depth under different initial saturations. (a) BI test blocks. (b) BII test blocks.

penetration depth under the same conditions. This is because that k_s^c increases with crack width (formula (6)); hence, the water velocity u^c increases with crack width w (formula (7)), which results in the fast growth of concrete saturation s . Then, the saturation difference with initial saturation became greater, and as a result, penetration depth is more obvious on the surface of the test block. In addition, the penetration depths of BI and BII blocks with the same crack width and similar initial saturation are close, the difference of which is less than those in Figures 7 and 8.

4. Numerical Analysis

EOS9 module of TOUGH2 (transport of unsaturated groundwater and heat) software was used to run water transport in the cracked BI block, which can simulate saturated and unsaturated flows in porous media [26]. Considering the symmetry of the test block (Figure 1), only half of the test block was modeled. Fracture was set at $y=35.5 \text{ mm}$ and $z=(0-100) \text{ mm}$ of the model, and the grid within 20 mm around the crack was densely meshed (Figure 10). The porosity and initial saturation of the crack

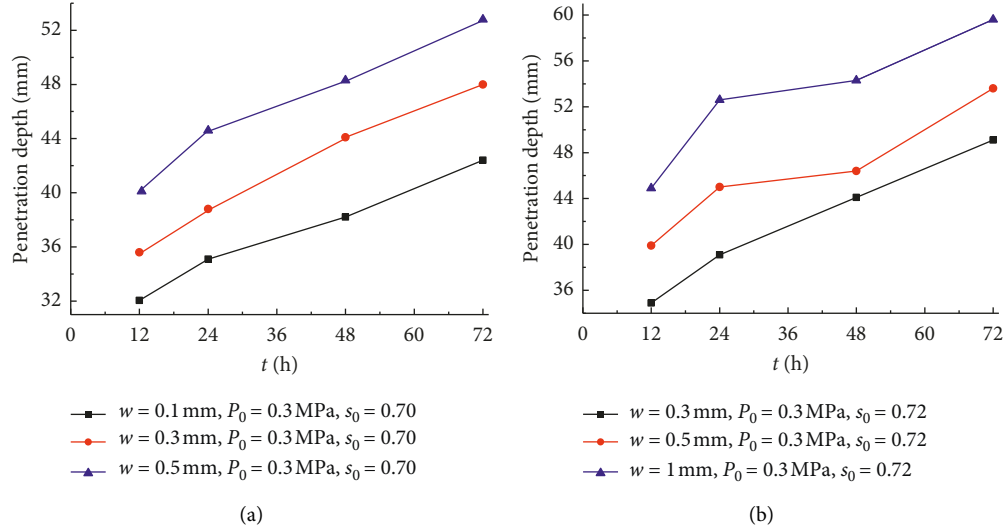


FIGURE 9: Penetration depth under different crack widths. (a) BI test blocks. (b) BII test blocks.

were taken as 0.99 and 0.7, and the intrinsic permeability coefficient of the crack was calculated by using formula (6). The prefabricated hole at the bottom of the crack was set as injecting boundary of the model, which was subjected to external water pressure P_0 with different water velocities (Darcy's law). The rest meshed elements were set as concrete, porosity, initial saturation, and saturated hydraulic conductivity of which were taken from the foregoing experiments. Empirical parameters α and m were taken as 9.662 MPa and 0.519 according to the literature [25].

4.1. Change of Model Saturation. Taking the working conditions 1–4 as an example, simulated saturation of the model is shown in Figure 11. It can be seen that the crack reaches full saturation first due to its large permeability coefficient, while the saturation far from the crack is basically equal to the initial saturation s_0 at $t = 12$ h. Then, the saturation gradually increases and expands around the crack and inlet hole, which reflects the water movement in concrete. The shape of saturation distribution is similar to that of the experimental penetration depth map.

4.2. Change of Driving Potential. Figure 12 shows the simulated pressure potential and matric potential of the working conditions 1 and 4. It is easily found that the scope of pressure potential is small and expands with time, while the scope of matric potential covers most of the model and the absolute value of matric potential decreases with time. The change of the two potentials indicates that the driving force of water transport is converted with the increase of water saturation. It is worthy to note that the absolute value of matric potential is much greater than that of pressure potential; hence, the matric potential plays an important role in water transport of underwater unsaturated concrete structures.

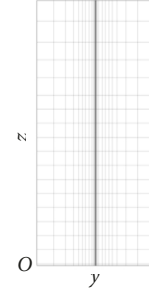


FIGURE 10: Mesh diagram of the model.

4.3. Change of Water Flow Velocity. Based on the parameters of working conditions 1, 5, 9, 13, and 21, the water flow velocity of the model under different working conditions was numerically analyzed, and the simulated velocity diagram at $z = 50$ mm is shown in Figure 13. It is found that flow velocity displays an antisymmetric distribution around the crack, because the directions of water flow on both sides of the crack are just opposite. Since water infiltrates concrete from the more permeable crack, the absolute velocity at the crack is the fastest, while the velocity far from the crack is low and almost zero at the first 12 h. In general, the greater the external pressure, the lower the initial saturation, and the larger the crack width, the greater the water velocity. Hence, it results in more water infiltration and saturation increase, which is in agreement with the experimental analysis in Section 3.4. With the time going, the maximum velocity near the crack decreases gradually, while the velocity far from the crack gradually increases due to water transport and then the velocity difference between the inner and outer boundaries slows down.

5. Conclusion

Considering the high pressure of underwater tunnels and unsaturated characteristics of concrete, theoretical models of

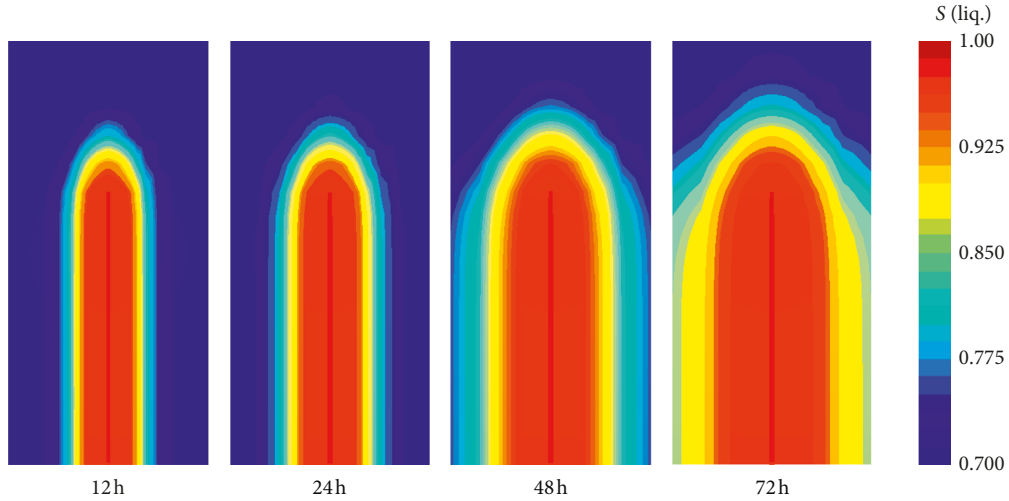


FIGURE 11: Simulated saturation profiles of working conditions 1–4.

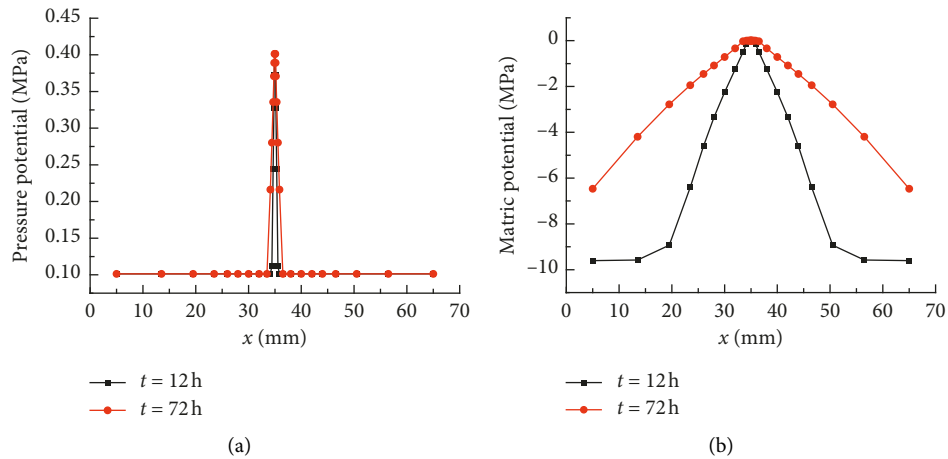


FIGURE 12: Simulated driving potential of working conditions 1 and 4. (a) Pressure potential. (b) Matric potential.

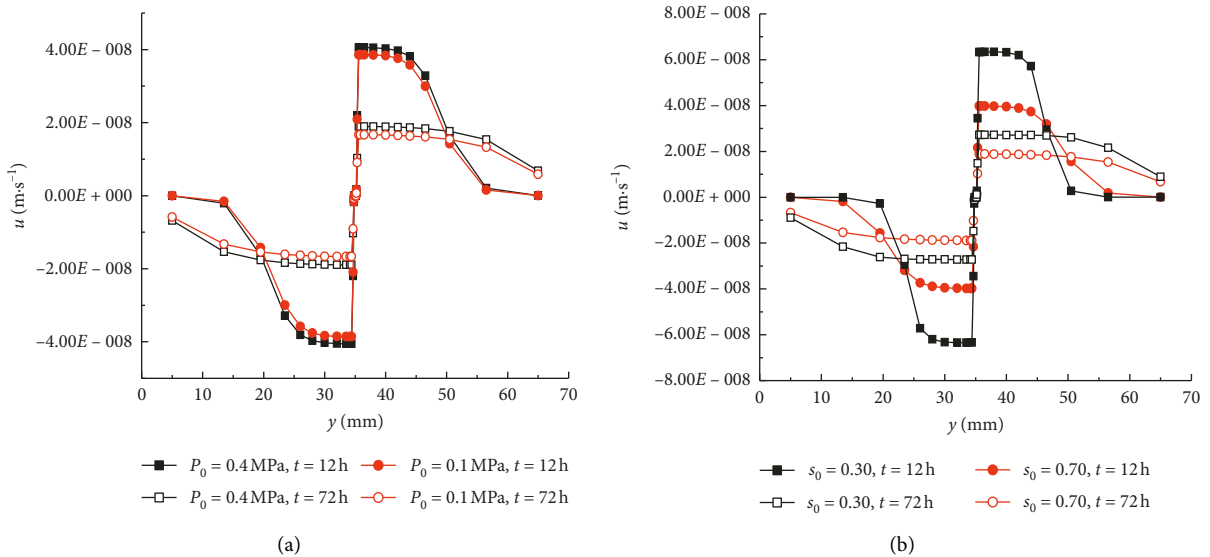


FIGURE 13: Continued.

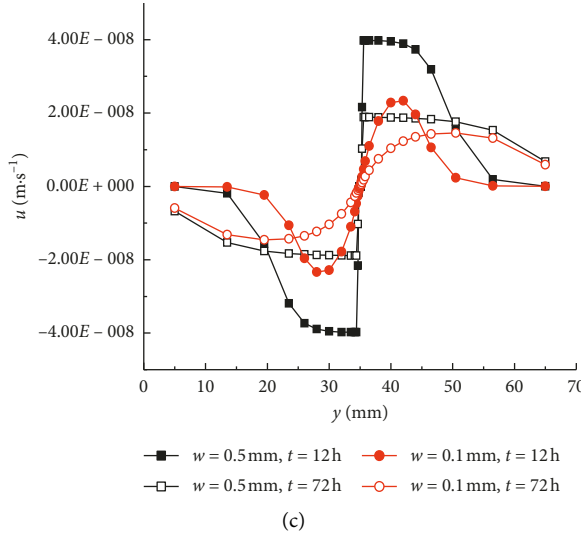


FIGURE 13: Simulated flow velocity under different working conditions and under (a) different water pressures, (b) different initial saturations, and (c) different crack widths.

water transport in unsaturated cracked concrete under pressure were established based on Richards' equation and the cubic law. The variation of penetration depth with pressuring time, hydraulic pressure, initial saturation, and crack width was investigated through penetration tests under hydraulic pressure. Moreover, the change and distribution of water saturation, driving potential, and flow velocity were numerically analyzed using TOUGH2 software. The results show that the larger the water pressure, the lower the initial saturation, and the greater the crack width, then the deeper the penetration depth of concrete. The water motion theoretical models proposed in this study can reasonably explain the process of water transport in unsaturated cracked concrete under pressure, which is in agreement with the experimental and numerical results. It indicates that the driving force of water motion is converted from matric potential in the unsaturated zone to pressure potential in full saturated zone, and the greater difference of driving potential results in faster growth of water content and deeper penetration depth of concrete. The research is helpful to improve the durability design of the underwater concrete tunnel.

Data Availability

The data used to support the findings of this study are included within the article.

Conflicts of Interest

The authors declare that they have no conflicts of interest.

Acknowledgments

This work was supported by the National Natural Science Foundation of China (Grant no. 51878609) and the Natural

Science Foundation of Zhejiang Province of China (Grant nos. LY17E080004 and LY18E080026).

References

- [1] K. Miyaguchi, "Maintenance of the Kanmon railway tunnels," *Tunnelling and Underground Space Technology*, vol. 1, no. 3-4, pp. 307–314, 1986.
- [2] H. Baji, C.-Q. Li, S. Sciluna, and J. Dauth, "Risk-cost optimised maintenance strategy for tunnel structures," *Tunnelling and Underground Space Technology*, vol. 69, pp. 72–84, 2017.
- [3] H. A. Russell and J. Gilmore, *Inspection Policy and Procedures for Rail Transit Tunnels and Underground Structures*, National Academy Press, Washington, DC, USA, 1997.
- [4] A. Kermani, "Permeability of stressed concrete," *Building Research Information*, vol. 19, no. 6, pp. 123–135, 1991.
- [5] B. Gérard, D. Breysse, A. Ammouche, O. Houdusse, and O. Didry, "Cracking and permeability of concrete under tension," *Materials and Structures*, vol. 29, no. 3, pp. 141–151, 1996.
- [6] K. Wang, D. C. Jansen, S. P. Shah et al., "Permeability study of cracked concrete," *Cement and Concrete Research*, vol. 27, no. 3, pp. 37–84, 1997.
- [7] V. Picandet, A. Khelidj, and H. Bellegou, "Crack effects on gas and water permeability of concretes," *Cement and Concrete Research*, vol. 39, no. 6, pp. 537–547, 2009.
- [8] G. Rastiello, C. Boulay, S. Dal Pont, J. L. Tailhan, and P. Rossi, "Real-Time water permeability evolution of a localized crack in concrete under loading," *Cement and Concrete Research*, vol. 56, no. 2, pp. 20–28, 2014.
- [9] S.-T. Yi, T.-Y. Hyun, and J.-K. Kim, "The effects of hydraulic pressure and crack width on water permeability of penetration crack-induced concrete," *Construction and Building Materials*, vol. 25, no. 5, pp. 2576–2583, 2011.
- [10] K. J. Shin, W. Bae, S.-W. Choi, M. W. Son, and K. M. Lee, "Parameters influencing water permeability coefficient of cracked concrete specimens," *Construction and Building Materials*, vol. 151, pp. 907–915, 2017.

- [11] L. Wang, J. Bao, and T. Ueda, "Prediction of mass transport in cracked-unsaturated concrete by mesoscale lattice model," *Ocean Engineering*, vol. 127, no. 15, pp. 144–157, 2016.
- [12] C. Leech, D. Lockington, and P. Dux, "Unsaturated Diffusivity functions for concrete derived from NMR images," *Materials and Structures*, vol. 36, no. 7, pp. 413–418, 2003.
- [13] C. K. Edvardsen, "Deterioration modelling model verification through in-situ tests great belt link tunnel (Denmark). Safe & Reliable Tunnels," in *Proceedings of the First International Symposium, Safe & Reliable Tunnels, Innovative European Achievements*, pp. 177–184, Prague, Czech Republic, February 2004.
- [14] J. E. Warran and P. J. Root, "The behaviour of naturally fractured reservoirs," *Society of Petroleum Engineers*, vol. 3, pp. 245–255, 1963.
- [15] L. A. Richards, "Capillary conduction of liquids through porous mediums," *Physics*, vol. 1, no. 5, pp. 318–333, 1931.
- [16] M. T. Van Genuchten, "A closed-form equation for predicting the hydraulic conductivity of unsaturated soils," *Soil Science Society of America Journal*, vol. 44, no. 5, pp. 892–898, 1980.
- [17] J.-H. Yoo, H.-S. Lee, and M. A. Ismail, "An analytical study on the water penetration and diffusion into concrete under water pressure," *Construction and Building Materials*, vol. 25, no. 1, pp. 99–108, 2011.
- [18] E. Lemarchand, C. A. Davy, L. Dormieux, W. Chen, and F. Skoczyłas, "Micromechanics contribution to coupled transport and mechanical properties of fractured geo-materials," *Transport in Porous Media*, vol. 79, no. 3, pp. 335–358, 2009.
- [19] GB/T 50081–2002, *Standard for Test Method of Mechanical Properties on Ordinary Concrete*, China Architecture & Building Press, Beijing, China, 2003, in Chinese.
- [20] ASTM C 642-13, *Standard Test Method for Density, Absorption, and Voids in Hardened Concrete*, Annual Book of ASTM Standards, Philadelphia, PA, USA, 2013.
- [21] SL352–2006, *Test Code for Hydraulic Concrete*, China Electric Power Press, Beijing, China, 2006, in Chinese.
- [22] M. N. Chari and M. Shekarchizadeh, "A simplified method for determination of the moisture transfer coefficient of concrete," *International Journal of Civil Engineering*, vol. 15, no. 8, pp. 1131–1142, 2017.
- [23] P. Zhang, F. H. Wittmann, T. Zhao, and E. H. Lehmann, "Neutron imaging of water penetration into cracked steel reinforced concrete," *Physica B: Condensed Matter*, vol. 405, no. 7, pp. 1866–1871, 2010.
- [24] N. Tsuchiya, M. Kanematsu, and T. Noguchi, "Quick water movement around concrete cracks under unsaturated conditions," *Construction and Building Materials*, vol. 67, pp. 95–99, 2014.
- [25] Y. Z. Zhang, X. Z. Li, X. J. Wei et al., "Water penetration in underwater concrete tunnel," *Journal Chinese Ceramic Society*, vol. 43, no. 4, pp. 368–375, 2015, in Chinese.
- [26] K. C. Pruess, C. M. Oldenburg, and G. J. Moridis, *TOUGH2 User's Guide, Lawrence Berkeley National Laboratory Report*, Lawrence Berkeley National Laboratory, Berkeley, CA, USA, 1999.

